

Antiphase Domain Boundary Formation in 2D Ba–Ti–O on Pd(111): An Alternative to Phase Separation

Friederike Elisa Wühl, Oliver Krahn, Sebastian Schenk, Stefan Förster,*
and Wolf Widdra

2D oxide quasicrystals (OQCs) are unique structures arising from atoms positioned at the vertices of a dodecagonal triangle–square–rhombus tiling. The prototypical example for OQCs is derived from BaTiO₃ on Pt(111). Herein, scanning tunneling microscopy (STM) and low-energy electron diffraction (LEED) investigations of 2D oxide layers derived from BaTiO₃ on Pd(111) are reported. Upon ultrahigh vacuum (UHV) annealing, different long-range ordered structures are observed with a base of four vertex atoms forming two edge-sharing equilateral triangles. By a periodic repetition of this base in either quadratic or rectangular unit cells, a triangle–square tiling (known as σ -phase approximant or 3².4.3.4 Archimedean tiling) or a triangle–rhombus tiling is formed. Both structures vary strongly in their vertex density. In addition, the formation of antiphase domain boundaries in the σ phase is observed resulting in a well-ordered incorporation of rhombuses in the triangle–square tiling. A systematic variation of the frequency of these domain boundaries is identified as a mechanism for an incremental increase in the global vertex density, mediating between pure triangle–square and triangle–square–rhombus tilings.

1. Introduction

The discovery of a quasicrystalline phase in ultrathin films derived from BaTiO₃ on Pt(111) opened a new field of research for ternary oxides on metal substrates.^[1] These oxide quasicrystals (OQCs) are the first observation of spontaneous formation of long-range ordered dodecagonal structures on-top of hexagonal substrates. The dodecagonal structure results from a close-packed tiling of equilateral triangles, squares, and rhombuses that had been theoretical defined as dodecagonal Niizeki-Gähler tiling, a quarter century before the first experimental evidence.^[1–5] In the OQC, the cation species which shows strong


contrast in atomically resolved STM decorates all vertex positions of the dodecagonal tiling. The full structure of the OQC is not yet solved, which is why an assignment of the STM contrast to either Ti or Ba atoms remains currently a matter of debate.^[6,7] In the context of the OQC, several periodic approximant structures have been reported which share common tiling elements of the parent OQC. Upon variations of the preparation conditions of BaTiO₃-derived films on Pt(111), such periodic structures are observed as a consequence of compositional changes affecting the vertex density.^[6–12] While some structures have been successfully prepared as single phases, also the coexistence of phases of varying vertex density in neighboring domains has been reported.^[8] This phase separation mechanism is commonly observed upon compositional changes, e.g., in monolayer oxides^[13–16] and in metal–organic coordina-

tion networks,^[17] or for coverage variations in noble gas adlayers^[18] and self-assembled molecular layers.^[19,20]

To elucidate the role of the lattice mismatch between the parent ternary oxide and the metal support toward the stabilization of dodecagonal oxide layers, different oxide layer/substrate combinations have been studied previously.^[5,21] Between BaTiO₃ and Pt, which are the two components forming the prototypical OQC, the lattice mismatch amounts to -2.0% . So far, mismatches of -4.5% and vanishing mismatch conditions have been realized by combining BaTiO₃ with Ru(0001) and SrTiO₃ with Pt(111), respectively.^[5,21] In both cases, a strong epitaxial stabilization of periodic structures is found. For BaTiO₃/Ru(0001), a commensurate triangle–square tiling known as σ -phase approximant or 3².4.3.4 Archimedean tiling is observed.^[5] For SrTiO₃/Pt(111), a more complex triangle–square–rhombus tiling forms a commensurate phase.^[21]

Here, we report on the structure evolution in ultrathin oxide layers derived from BaTiO₃ on Pd(111). For this material combination, a nominal lattice mismatch of -2.8% can be calculated, close to the conditions in BaTiO₃/Pt(111). Upon annealing in UHV at 930 to 1030 K, reduced Ba–Ti–O forms long-range ordered 2D layers on the Pd substrate. In these wetting layers, a series of structures is identified by means of STM and LEED. In this report, we will focus on single-phase structures with small unit cells. One of these structures is the σ phase, which is a quadratic structure with a base of four vertex atoms.

F. E. Wühl, O. Krahn, S. Schenk, S. Förster, W. Widdra
Institute of Physics
Martin-Luther-Universität Halle-Wittenberg
Halle D-06099, Germany
E-mail: stefan.foerster@physik.uni-halle.de

 The ORCID identification number(s) for the author(s) of this article can be found under <https://doi.org/10.1002/pssb.202100389>.

© 2021 The Authors. physica status solidi (b) basic solid state physics published by Wiley-VCH GmbH. This is an open access article under the terms of the Creative Commons Attribution License, which permits use, distribution and reproduction in any medium, provided the original work is properly cited.

DOI: 10.1002/pssb.202100389

In the second long-range ordered phase the same four vertex are periodically repeated in a rectangular unit cell. As a consequence, the vertex density is strongly increased. Finally, modifications of the σ phase are observed in which σ -phase patches are connected by periodic antiphase domain boundaries, thus realizing intermediate vertex densities.

2. Results

Ultrathin films of Ba–Ti–O have been deposited by exposing the clean Pd(111) surface at room temperature subsequently to Ba and Ti vapor. Upon post-annealing at 770 K in 10^{-5} mbar O_2 , this mixed metal layer is fully oxidized. The chemical nature of these films has been investigated by means of X-ray photoelectron spectroscopy (XPS). **Figure 1** shows exemplarily the Ba 3d and Ti 2p core-level regions for a 5 Å thin film of Ba–Ti–O. The film thickness has been determined from the damping of the Pd substrate peaks. The Ba 3d_{5/2} and Ti 2p_{3/2} core-level peaks are positioned at 780.3 and 458.0 eV, respectively, which is in good agreement to bulk BaTiO₃.^[22] Moreover, a first plasmon loss is observed in the Ti 2p region at 13.0 eV higher binding energy with respect to the 2p_{3/2} peak, which is also characteristic for BaTiO₃.^[22] Accounting for the differences in the escape depth of the Ba 3d and Ti 2p photoelectrons, a Ba:Ti composition of 0.5:1 has been

determined for the as prepared 5 Å thin layer. A higher initial Ti content has been chosen intentionally to compensate for Ti segregation into the Pd(111) bulk upon high-temperature treatment.^[23] Upon annealing, the ultrathin Ba–Ti–O at temperatures above 900 K in UHV, a second oxide species is formed at the surface, which is recognized most prominently in the Ti 2p region. The bottom spectra of Figure 1a shows the spectrum for the initially 5 Å thin Ba–Ti–O film upon multiple annealing cycles to a maximum temperature of 1030 K in UHV. In this spectrum, a second Ti 2p doublet (blue) shifted by 2.3 eV toward lower binding energies is seen indicating a reduction of the nominal oxidation state. However, the Ba 3d peak remains almost unchanged. Upon reduction, the Ba:Ti ratio of the Ba–Ti–O system reduces by 9%. A quantification of the oxygen content in the layer is not possible due to the superposition of the small O1s intensity with high intensities of the Pd 3p core-level peaks.

Figure 1b shows a large-scale STM image, which corresponds to the reduced state of the aforementioned preparation. In this image, two different oxide species become evident in the morphology of the Ba–Ti–O layer on the Pd(111) surface. On the one hand, islands of different sizes are decorating the substrate step edges, that appear with a rough surface in STM (marked by I in Figure 1b). These islands are attributed to fully oxidized stoichiometric BaTiO₃. On the other hand, extended smooth terraces exist, that are fully encapsulated with layers of different structure, which will be introduced in the following text. Following the assumption of a Ba:Ti ratio of 1:1 for the BaTiO₃ islands, the global change of the Ba:Ti ratio by 9% upon reduction is indicative for a Ba:Ti composition of the reduced oxide layer significantly below 0.5:1.

The observed behavior is typical for ultrathin ternary oxide films on metal support and has been characterized in 2D Ba–Ti–O films on Pt(111) before, see ref. [24]. The fully oxidized ternary oxide tends to form 3D perovskite islands upon annealing and, therefore, to dewet the metal surface between the islands. Under reducing conditions, a reduced oxide layer is formed starting at a threshold temperature, which fully covers the metal substrate in-between remaining 3D bulk-like islands.^[25] Studies of Sr–Ti–O films on Pt(111) and Ba–Ti–O films on Ru(0001) report a similar phenomenon.^[5,21]

The fully oxidized Ba–Ti–O films on Pd(111) annealed at 770 K in 10^{-5} mbar O_2 do not possess any long-range order in LEED. However, a variety of long-range ordered structures are present upon annealing in UHV, which will be introduced in the following. The onset of long-range order in the reduced oxide has been observed upon annealing at 930 K for 10 min. **Figure 2** shows the corresponding LEED pattern. In addition to the very intense spots of the hexagonal Pd(111) substrate at 2.64 \AA^{-1} a ring is visible at 2.41 \AA^{-1} in the diffraction pattern of Figure 2a. For Ba–Ti–O on Pt(111), a similar ring has been observed indicating the formation of a 2D reduced oxide wetting layer, which is initially poorly ordered.^[25,26] Furthermore, a long-range ordered structure is present that gives rise to sharp superstructure spots in LEED. This superstructure is characterized by 12 intense spots at an reciprocal distance of 1.00 \AA^{-1} around the origin of the diffraction pattern and around each of the first-order substrate spots. All these spots are related to a $\begin{pmatrix} 1 & 3 \\ 5 & 1 \end{pmatrix}$ superstructure with respect to Pd(111). It is a rectangular structure with unit

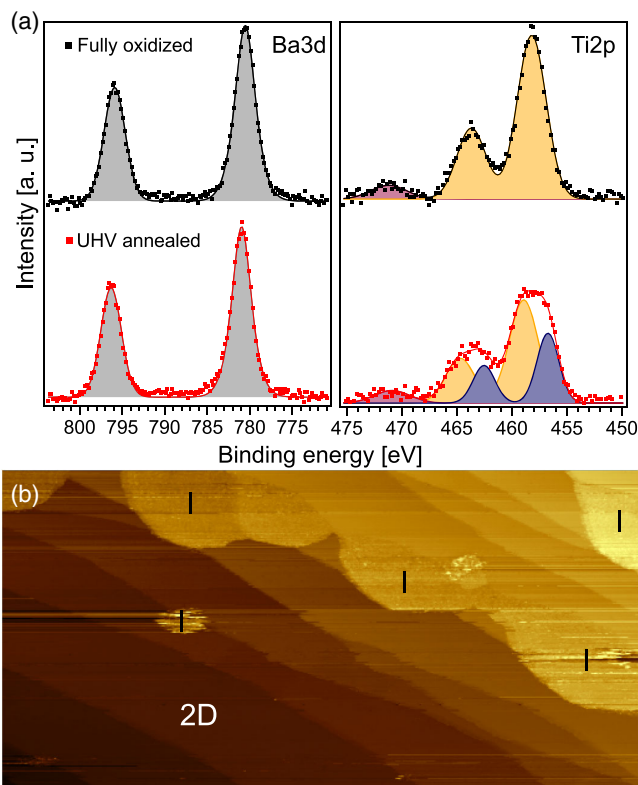


Figure 1. a) XPS spectra of 5 Å Ba–Ti–O on Pd(111) upon full oxidation (top) and UHV annealing (bottom). b) Large-area STM image of the sample upon UHV annealing showing the presence of islands (I) on planar terraces which are covered by a reduced 2D oxide. The different structures formed in this 2D layer will be discussed in the text. b) $500 \times 250 \text{ nm}^2$, 0.4 Å, 2.0 V, $\Delta z = 2.8 \text{ nm}$.

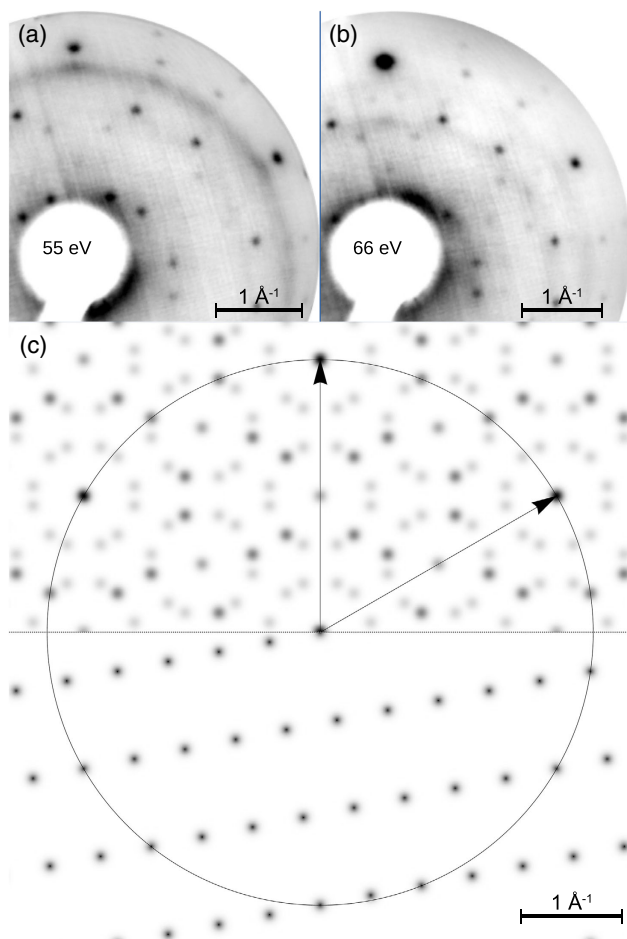


Figure 2. a,b) LEED pattern of 5 Å Ba–Ti–O on Pd(111) upon annealing at 930 K for 10 min in UHV. c) Simulated pattern for a single domain of a rectangular $\begin{pmatrix} 1 & 3 \\ 5 & 1 \end{pmatrix}$ superstructure on Pd(111) (bottom) and the substrate-induced superposition of six rotational and mirror domains (top) reproducing the measured pattern.

vectors of 12.6 and 7.3 Å. The latter is rotated by 19.1° against the substrate. A simulated diffraction pattern of a single domain of this structure is shown in the lower part of Figure 2c. Due to a lack of STM data giving the unit cell filling, only the unit cell dimensions have been considered. As a consequence of the substrate symmetry, three different rotational and three mirror domains occur. The simulated pattern for a superposition of all six domains is shown in the upper part of Figure 2c. In this pattern intensity differences arise from coinciding spots of different domains. The spots of higher intensities are the ones dominating the measured LEED patterns of Figure 2a,b.

Upon further annealing of this film for 60 min at 930 K, the 2D oxide layer covers the Pd(111) terraces as shown by the STM image of Figure 3a. In this densely packed atomic arrangement an almost quadratic array of elongated protrusions can be recognized. Along the two almost perpendicular rows of this grid, neighboring protrusions are rotated by 90° with respect to each other. The close-up STM image in Figure 3b shows that these elongated shapes result

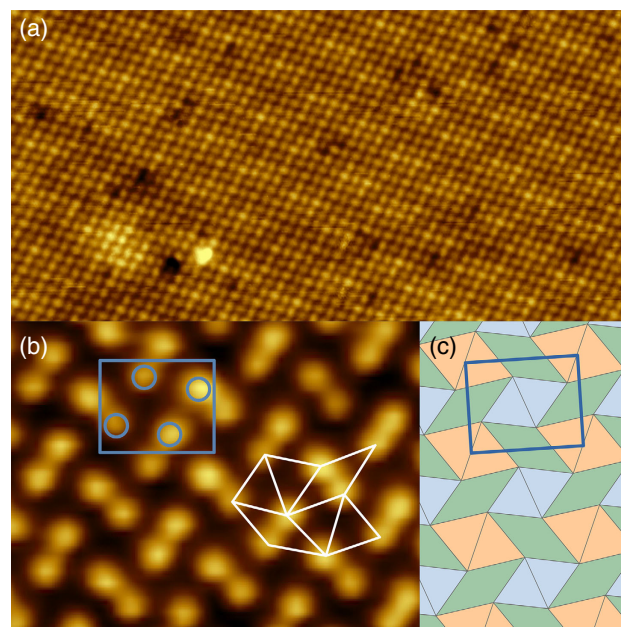


Figure 3. STM data of 5 Å Ba–Ti–O on Pd(111) upon annealing at 930 K for 60 min in UHV. a) Large-scale image revealing a homogeneous patterning of the Pd(111) terraces. b) Close-up STM image identifying a rectangular cell with a base of four vertices. c) Schematic representation of the resulting tiling formed from smaller triangles (blue) and larger triangles (orange) and rhombuses with inner angles of 40° and 140°. a) 46 × 23 nm², 0.3 A, 1.2 V, Δz = 140 pm. b) 10.5 × 8.0 nm², 0.1 A, 1.2 V, Δz = 30 pm.

from two protrusions in close vicinity. This structure can be described by a rectangular unit cell that includes a base of four protrusions (marked blue in Figure 3b). The protrusions decorate the vertices of two edge-sharing equilateral triangles. The periodic repetition of this atomic base results in the formation of a second pair of triangles with a 10% larger edge length, which is rotated by 40° against the base. This is shown in the scheme of Figure 3c, in which the small triangles are colored in blue and the larger ones in orange. The remaining voids (green) are rhombuses with inner angles of 40° and 140°. From this scheme, the characteristic building blocks of the tiling can be derived. It consists of two double triangles and two rhombuses of different rotations, as shown in white in Figure 3b. In the larger area STM image in Figure 3a, a moiré pattern is induced from small height variations. A comprehensive analysis of the moiré pattern is provided in the Supporting Information.

Figure 4a,b shows the LEED pattern recorded for this rectangular structure at different electron kinetic energies. Most prominent is a set of three spots with an alternating angular spacing of 28° and 32° centered at a reciprocal distance of 1.2 Å. In addition, 12 or 24 spots are observed at various radii. Therefore, a rotation of the rectangular unit cell out of the mirror planes of the hexagonal substrate can be concluded. The measured diffraction pattern is perfectly reproduced in simulations using a $\begin{pmatrix} 16/3 & 4/3 \\ 11/9 & 38/9 \end{pmatrix}$ superstructure with respect to Pd(111). Figure 4c shows the simulated pattern of a single domain (bottom) and the superposition of all six rotation and mirror domains (top). By including the base of four atoms as determined from STM, the calculated intensities nicely agree with the measured ones. This is remarkable as only

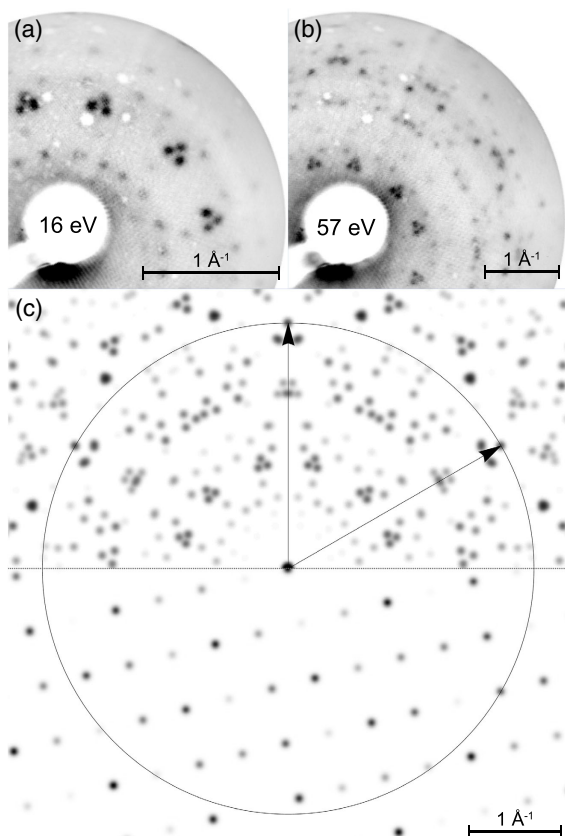


Figure 4. a,b) LEED pattern of a rotated rectangular superstructure formed in 5 Å Ba–Ti–O on Pd(111) upon annealing at 930 K for 60 min in UHV. c) Simulated pattern for a single domain of the rectangular structure (bottom) and the superposition of six domains (top).

one subgrid of atoms of this ternary compound can be detected by STM, although all atomic species contribute in LEED.^[6,7] The given matrix corresponds to a higher-order commensurate structure with unit vectors of 13.2 and 10.3 Å inclining an angle of 89.8°. This structure is rotated by 13.9° against the substrate. The matrix is perfectly in line with the observed moiré pattern in STM data: substrate registry is achieved in one direction by three repetitions of the long unit vector. In the other direction, a linear combination of one long unit vector and three repetitions of the short unit vector are needed. Further explanation is available in the Supporting Information.

Upon multiple cycles of oxygen and UHV annealing with an final annealing step for 30 min to 1020 K, the wetting layer structure changes into the σ phase, which has been reported for Ba–Ti–O on Pt(111) and Ru(0001) before.^[5,6,27] This structure is a simple triangle–square tiling, as shown in the STM image in Figure 5a.

The unit cell is quadratic and contains a base of four vertex atoms (marked blue in Figure 5a). These four vertices are arranged in a similar fashion as found for the rectangular structure described earlier. It results in a characteristic tiling consisting of four triangles and two squares (white in Figure 5a). In the STM image of the σ phase in Figure 5a, a 1D moiré structure is

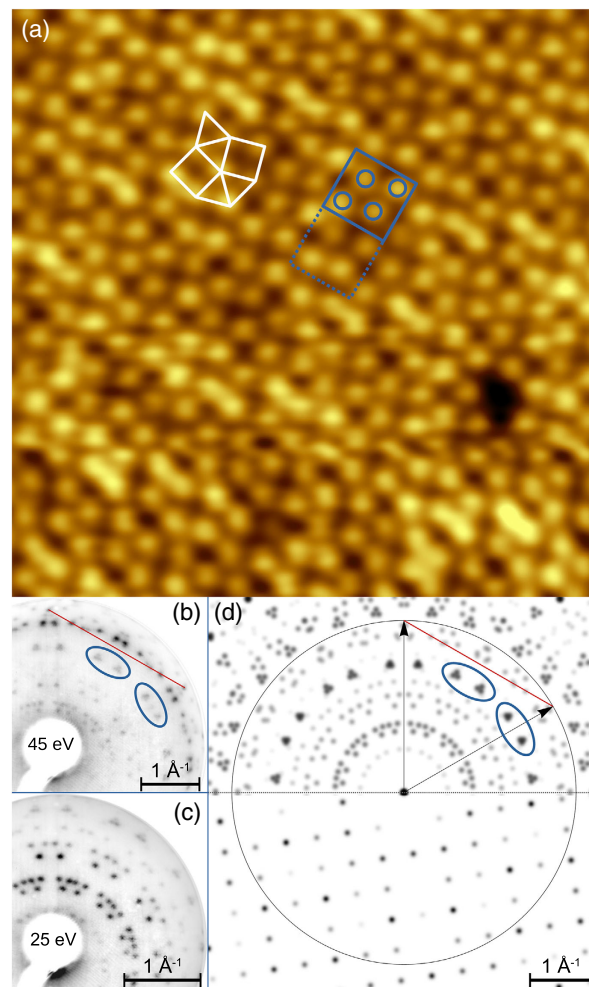


Figure 5. a) STM and b–d) LEED data of the σ phase in Ba–Ti–O on Pd(111). The quadratic unit cell and the base of four atoms are marked in blue. The characteristic building block of the triangle–square tiling resulting from the periodic repetition of the base is marked in white. In this STM image, a stripe-like moiré pattern is seen having a periodicity of two unit cells as emphasized by the dashed lines. b,c) Experimentally observed LEED pattern of the σ phase and d) the simulated pattern for a single domain (bottom) and the superposition of six domains (top). a) 11 × 11 nm², 100 pA, 1.0 V, $\Delta z = 150$ pm.

present. In an alternating fashion, two rows of atoms running from the upper left to the lower right of Figure 5a appear brighter, whereas the next two rows are dimmer.

This 1D moiré has a periodicity of twice the lattice parameter of the σ -phase unit cell. The σ phase exhibits a very characteristic LEED pattern, which is shown in Figure 5b,c. At various reciprocal distances, 24 groups of three spots each are observed. The simulated pattern of this structure is shown in Figure 5d. The structure is determined by a $\begin{pmatrix} 31/6 & 5/6 \\ 2 & 11/2 \end{pmatrix}$ superstructure matrix with respect to Pd(111). The perfect agreement between the simulated and measured LEED pattern is seen best in the reproduction of the tiny differences in the splitting of the triangles generated by the fifth- and sixth-order spots marked in blue in

Figure 5b,d and the spots cut by the connecting line of the first-order substrate spots marked in red. The unit vectors derived from this superstructure matrix are 13.2 and 13.3 Å in length inclining a 90.3° angle. This results in a next-neighbor distance of 6.85 Å in the triangle–square tiling. The unit cell is rotated by 8.6° against the substrate. As read from the superstructure matrix, a period doubling along the second unit vector of the σ phase results in a snap-into-registry with the substrate, which is in-line with the observed moiré pattern. The configuration of the σ phase on Pd(111) is very close to what has been reported for Pt(111).^[6,27] There, the unit cell is slightly compressed along one unit vector, the inner angle is slightly larger, and the rotation against the substrate is reduced to 8°. However, as the differences are small, the LEED pattern are almost indistinguishable for the different substrates. In contrast, on the Ru(0001) substrate the σ phase unit cell is rotated by 15° against the substrate.^[5]

In contrast to Ba–Ti–O on all other investigated substrates, local modifications of the σ phase are observed on Pd(111). **Figure 6a** shows a large-scale STM image that demonstrates a high level of perfection in the long-range order of the σ phase. Only two adatoms (bright spots) and a single vacancy (dark hole) are seen in the entire image containing more than 5000 vertices. The second detail to note are compact lines of atoms running in vertical direction. The close-up STM image in **Figure 6b** shows that these compact rows are created by vertically stacked rhombuses inclining 30° and 150° angles. These rows of rhombuses are enclosed on both sides by a variable number of σ -phase unit cells as marked by white squares in **Figure 6a**. These σ -phase unit cells are shown in **Figure 6b** in red and yellow. Both domains are oriented in the same direction, but exhibit a lateral offset of half a unit vector in vertical direction and $\sqrt{3}/2$ perpendicular to it (marked by blue lines in **Figure 6b**). The phase shift of half a σ -phase unit cell along the domain boundary corresponds to the condition of 1D antiphase domain boundaries. The phase shift across the domain boundary of a $\sqrt{3}/2$ unit cell, however, allows sharing of two (out of four) vertex positions between both domains. As the domain width is only $\sqrt{3}/2$ unit cell wide and contains also four vertex atoms, the domain boundary is denser than the σ phase on both sides. This higher density of vertices results in the formation of rhombuses as new tiling elements. The new characteristic tiling motif generated by this antiphase domain boundary is emphasized in white in **Figure 6b**. The large-scale image in **Figure 6a** reveals that the number of σ -phase units between subsequent rows of rhombuses can vary. One, two, or four unit cells are found in this particular measurement. However, no repeating rule could be determined from the sequence of rows.

3. Discussion

In 2D layers of ternary oxides a variety of tilings arises from a combination of equilateral triangles, squares, and rhombuses. The most prominent example is the dodecagonal OQC, but also periodic structures ranging from simple to complex are known.^[1,6,8,21]

For 2D Ba–Ti–O on Pd(111), three different characteristic tiling motifs occur, as introduced earlier. These are the triangle–square patch of the σ phase, the triangle–square–rhombus patch observed at the antiphase domain boundaries, and the triangle–rhombus patch, which is an idealization of the motif found in the

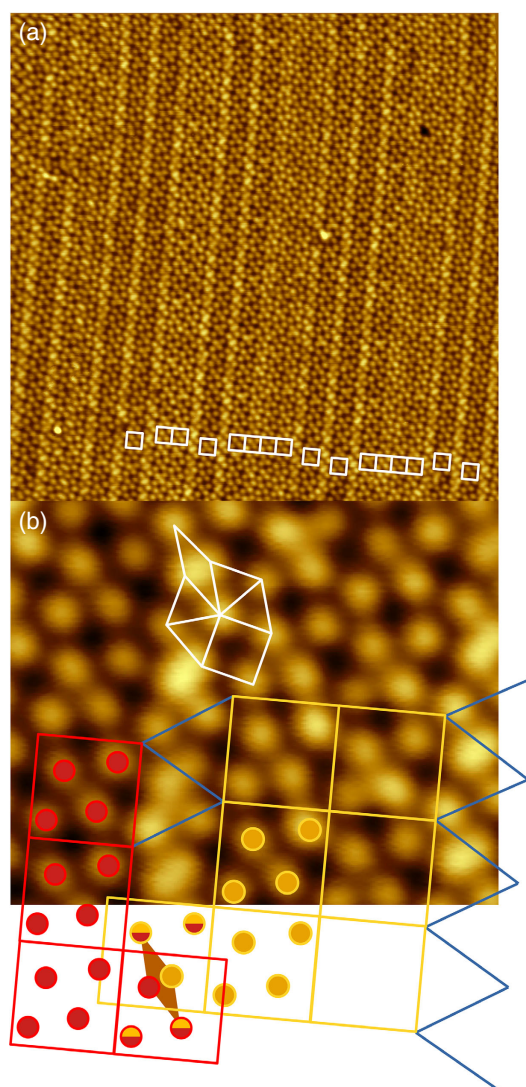


Figure 6. a) Large-scale STM image of σ -phase patches with incorporated rows of rhombuses. b) Schematics illustrating the formation of rhombuses as a result of 1D antiphase domain boundaries of neighboring σ -phase patches of identical orientation (red and yellow). a) $44 \times 44 \text{ nm}^2$, b) $6 \times 5 \text{ nm}^2$, a,b) 40 pA, 2.0 V, $\Delta z = 170 \text{ pm}$.

small aspect ratio rectangular structure shown in **Figure 3** and **4**. **Figure 7** shows, how all three tiling motifs can be traced back to the very same base of four vertices in different periodic repetitions. In **Figure 7a**, four vertices are arranged in a base such that they form two edge-sharing equilateral triangles. By periodically repeating this base in rectangular, quadratic, or hexagonal unit cells of appropriate size, periodic structures with different triangle–square–rhombus tiling motifs can be created. For the periodic repetition of all structures in **Figure 7a**, the unit vector length is $\sqrt{(2 + \sqrt{3})}$ times larger than the vertex separation and the unit vectors are rotated by 15° against the edges of the triangles. In case of the rectangular structure, this applies for the long unit vector only. The short unit vector has a length of $\sqrt{2}$ and is rotated by 45°. In the periodic repetition, new tiles are created by

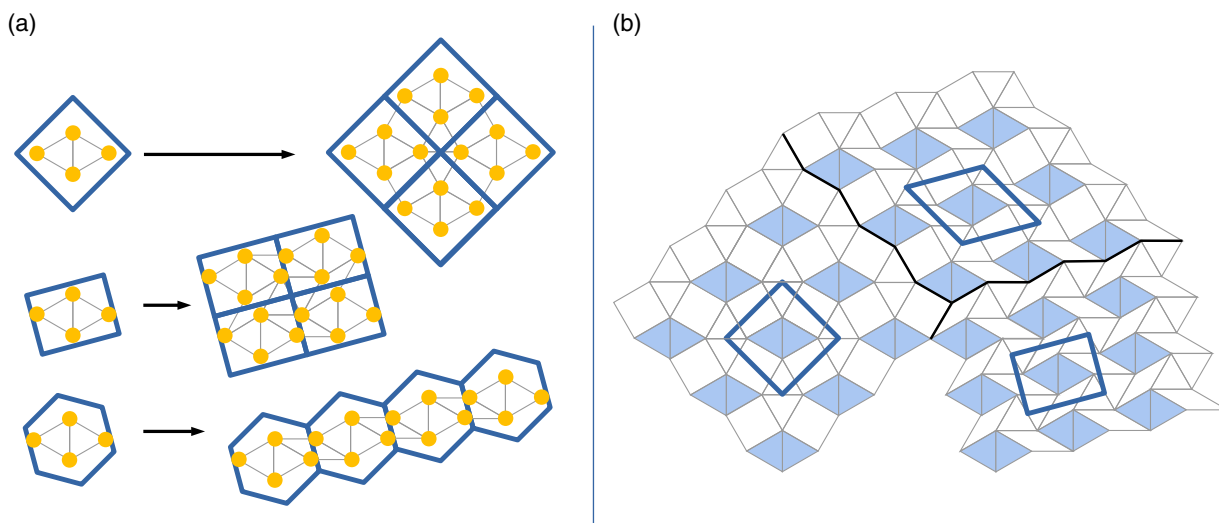


Figure 7. a) Three different structures that evolve from an identical base, which is periodically repeated in either quadratic, rectangular, or hexagonal fashion. The upper two examples resemble the σ phase and the rectangular structure observed in Ba–Ti–O on Pd(111), the lower one the conditions that apply at antiphase domain boundaries. b) The three tilings of (a) form smooth boundaries between extended patches. All three tilings are formed from tiles of constant edge length.

connecting the vertices across the unit cell boundaries. Due to the specific orientation of the base with respect to the unit vectors and the particular relation between the vertex separation and the unit cell dimensions, only triangles, squares, and rhombuses of constant edge length are formed. The magic factor of $\sqrt{2 + \sqrt{3}}$ is the inflation factor of the dodecagonal Niizeki–Gähler tiling, which produces a self-similar pattern under a rotation of 15° .^[2,3] While the upper two examples of Figure 7a exist in Ba–Ti–O on Pd(111) in extended patches in the rectangular structure and the σ phase, the bottom example periodically repeats in one dimension only along the antiphase domain boundaries between σ -phase patches. Due to the common unit vector length the three patches can be smoothly combined in neighboring domains, as shown in Figure 7b.

As an immediate consequence of the different unit cell areas, all three structures differ significantly in their vertex density. The pure σ phase exhibits the lowest density of 2.28 vertices per nm^2 . The density of the triangle–rhombus tiling in the rectangular structure amounts to 2.94 vertices per nm^2 . And the hypothetical hexagonal triangle–square–rhombus tiling would result in a density of 2.65 vertices per nm^2 . The inclusion of antiphase domain boundaries shown in Figure 6 can be rationalized in this context as a mechanism to accommodate an increasing vertex density in the σ phase. In the self-organized growth of 2D crystals of organic and inorganic materials, the formation of antiphase domain boundaries is observed frequently, which can produce denser or more dilute packing. At low temperatures, antiphase domain boundaries result from the intergrowth of immobilized nuclei.^[28] However, they also represent a way of releasing strain induced by increasing adsorbate coverages of organic and inorganic materials.^[29–32] In rare cases, they can be condensed into ordered arrays, thus forming a new structural phase as for surface layers of Pb and In.^[31,32] The latter scenario also applies for the ultrathin Ba–Ti–O layer on

Pd(111). The experimental observation of a variable spacing between subsequent domain boundaries indicates that the vertex density can be tuned in small increments. The minimum spacing between neighboring domain boundaries of one complete unit cell of the σ phase has been observed in experiments. This implies that based on the incorporation of domain boundaries, the vertex density can be tuned to a maximum of 2.45 vertices per nm^2 . We note that this maximum is equivalent to the vertex density in the Niizeki–Gähler tiling of the BaTiO₃-derived OQC on Pt(111). In other words, a periodic repetition of one σ -phase unit cell and the tiling motif formed at the antiphase domain boundary, resembles a similar vertex density, as given in the aperiodic Niizeki–Gähler tiling. While on Pt(111), the general scheme of demixing into phases of different composition is observed, which results in the coexistence of different structures in adjacent domains,^[8] the antiphase domain boundary formation on Pd(111) represents a fascinating alternative for mediating atom density variations.

4. Conclusion

The structure formation in ultrathin reduced layers of Ba–Ti–O on Pd(111) has been investigated. Three long-range ordered phases with small unit cells exist: two rectangular structures and the quadratic σ -phase approximant. One of the rectangular structure and the σ phase share a common base, which results in the formation of a triangle–rhombus and a triangle–square tiling, respectively. In contrast to other related systems, the incorporation of antiphase domain boundaries in the triangle–square tiling of the σ phase is observed on Pd(111). The systematic incorporation of domain boundaries is identified as a mechanism to tune the vertex density of the tiling from the low-density σ phase conditions toward that of the dodecagonal triangle–square–rhombus tiling found in OQC.

5. Experimental Section

Sample growth, LEED, and XPS measurements were carried out in an UHV system operating at a base pressure of 1×10^{-10} mbar. Pd(111) substrates (Mateck, Germany) were cleaned by repeated cycles of Ar⁺-ion sputtering at 1 keV and a two-step annealing process. In the first step, the crystal was briefly annealed at 1170 K for 30 s to heal out sputter-induced surface roughening. In the second step, the crystal was annealed at 900 K for 10 min at an oxygen partial pressure of 1×10^{-6} mbar. During the second step, residual carbon contaminations were oxidized to CO, which immediately desorbed at high temperatures. Due to the low sticking probability of oxygen on palladium at elevated temperatures, a clean metal surface was obtained. For temperature measurements, a pyrometer (Pyrospot DG40N, DIAS, $\lambda = 1600$ nm) was used at an emissivity of 0.17. Ba was supplied from a commercial Ba dispenser source (SAES Getters). Ti was evaporated from a rod out of a three-cell electron beam evaporator (Focus). Film thickness was estimated using a quartz crystal microbalance maintained at 345 K. Metal layers were deposited at room temperature and postoxidized by annealing in an oxygen atmosphere of 1×10^{-5} mbar for 20 min at 770 K. The XPS measurements were carried out using nonmonochromatized Al K α excitation. For detection, a 127° analyzer equipped with a single channeltron was used. From the measured data, Al K α satellites, an experimentally determined background of the bare substrate, and an additional Shirley background were subtracted prior to fitting. The XPS binding energy axis was calibrated to a Pd 3d5/2 core level energy of 335.2 eV.^[33] The STM measurements were carried out in a home-build STM. All measurements presented here were conducted at liquid nitrogen temperatures.

Custom code was used for LEED pattern calculation using point-like atoms under kinematic scattering with atomic form factor set to unity for all atoms, similar to earlier work.^[21] The unit cell base was defined according to the protrusions seen by STM. Calculated single domain patterns were further duplicated, symmetrically rotated, and mirrored according to the substrate symmetry. To compare the calculated pattern with experiment, the calculated intensities were plotted as 2D Gaussian profiles.

Acknowledgements

The authors thank R. Kulla for technical support. Financial support by the Deutsche Forschungsgemeinschaft (DFG) through the collaborative research center SFB 762 (Functionality of Oxide Interfaces, project A3) and the European Union (EFRE) is gratefully acknowledged.

Open access funding enabled and organized by Projekt DEAL.

Conflict of Interest

The authors declare no conflict of interest.

Data Availability Statement

Research data are not shared.

Keywords

2D ternary oxides, low-energy electron diffraction, oxide quasicrystals, scanning tunneling microscopy

Received: July 31, 2021

Revised: September 24, 2021

Published online: October 27, 2021

- [1] S. Förster, K. Meinel, R. Hammer, M. Trautmann, W. Widdra, *Nature* **2013**, *502*, 215.
- [2] N. Niizeki, H. Mitani, *J. Phys. A: Math. Gen.* **1987**, *20*, L405.
- [3] F. Gähler, in *Proc. of the ILL/CODEST Workshop*, World Scientific, Singapore **1988**, p. 13.
- [4] S. Schenk, E. M. Zollner, O. Krahn, B. Schreck, R. Hammer, S. Förster, W. Widdra, *Acta Crystallogr., Sect. A: Found. Adv.* **2019**, *75*, 307.
- [5] E. M. Zollner, F. Schuster, K. Meinel, P. Stötzner, S. Schenk, B. Allner, S. Förster, W. Widdra, *Phys. Status Solidi B* **2020**, *257*, 1900655.
- [6] S. Förster, M. Trautmann, S. Roy, W. A. Adeagbo, E. M. Zollner, R. Hammer, F. O. Schumann, K. Meinel, S. K. Nayak, K. Mohseni, W. Hergert, H. L. Meyerheim, W. Widdra, *Phys. Rev. Lett.* **2016**, *117*, 095501.
- [7] E. Cockayne, M. Mihalkovič, C. L. Henley, *Phys. Rev. B* **2016**, *93*, 020101.
- [8] S. Förster, K. Meinel, K.-M. Schindler, W. Widdra, *Surf. Interface Anal.* **2012**, *44*, 628.
- [9] J. Yuhara, K. Horiba, R. Sugiura, X. Li, T. Yamada, *Phys. Rev. Mater.* **2020**, *4*, 103402.
- [10] X. Li, K. Horiba, R. Sugiura, T. Yamada, J. Yuhara, *Appl. Surf. Sci.* **2021**, *561*, 150099.
- [11] T. T. Dorini, F. Brix, C. Chatelier, A. Kokalj, É. Gaudry, *Nanoscale* **2021**, *13*, 10771.
- [12] M. Maniraj, L. V. Tran, O. Krahn, S. Schenk, W. Widdra, S. Förster, *Phys. Rev. Mater.* **2021**, *5*, 084006.
- [13] C. Wu, M. S. J. Marshall, M. R. Castell, *J. Phys. Chem. C* **2011**, *115*, 8643.
- [14] F. Sedona, G. A. Rizzi, S. Agnoli, F. X. Llabrés i Xamena, A. Papageorgiou, D. Ostermann, M. Sambì, P. Finetti, K. Schierbaum, G. Granozzi, *J. Phys. Chem. B* **2005**, *109*, 24411.
- [15] C. Breinlich, M. Buchholz, M. Moors, S. L. Moal, C. Becker, K. Wandelt, *J. Phys. Chem. C* **2014**, *118*, 6186.
- [16] G. Barcaro, A. Fortunelli, *Phys. Chem. Chem. Phys.* **2019**, *21*, 11510.
- [17] J. Liu, T. Lin, Z. Shi, F. Xia, L. Dong, P. N. Liu, N. Lin, *J. Am. Chem. Soc.* **2011**, *133*, 18760.
- [18] M. Dunin von Przychowski, H. Wiechert, G. K. Marx, G. Schonhense, *Surf. Sci.* **2003**, *541*, 46.
- [19] G. E. Poirier, *Langmuir* **1999**, *15*, 1167.
- [20] U. Stahl, D. Gador, A. Soukopp, R. Fink, E. Umbach, *Surf. Sci.* **1998**, *414*, 423.
- [21] S. Schenk, S. Förster, K. Meinel, R. Hammer, B. Leibundgut, M. Paleschke, J. Pantzer, C. Dresler, F. O. Schumann, W. Widdra, *J. Phys.: Condens. Matter* **2017**, *29*, 134002.
- [22] L. T. Hudson, R. L. Kurtz, S. W. Robey, D. Temple, R. L. Stockbauer, *Phys. Rev. B* **1993**, *47*, 1174.
- [23] M. H. Farstad, D. Ragazzon, H. Groenbeck, M. D. Strömsheim, C. Stavrakas, J. Gustafson, A. Sandell, A. Borg, *Surf. Sci.* **2016**, *649*, 80.
- [24] S. Förster, S. Schenk, E. M. Zollner, O. Krahn, C.-T. Chiang, F. O. Schumann, A. Bayat, K.-M. Schindler, M. Trautmann, R. Hammer, K. Meinel, W. A. Adeagbo, W. Hergert, J. I. Flege, J. Falta, M. Ellguth, C. Tusche, M. DeBoissieu, M. Muntwiler, T. Greber, W. Widdra, *Phys. Status Solidi B* **2020**, *257*, 1900624.
- [25] S. Förster, J. I. Flege, E. M. Zollner, F. O. Schumann, R. Hammer, A. Bayat, K.-M. Schindler, J. Falta, W. Widdra, *Ann. Phys. (Berlin)* **2017**, *529*, 1600250.
- [26] S. Förster, W. Widdra, *Surf. Sci.* **2010**, *604*, 2163.

- [27] S. Roy, K. Mohseni, S. Förster, M. Trautmann, F. Schumann, E. Zollner, H. Meyerheim, W. Widdra, *Z. Kristallogr.—Crystall. Mater.* **2016**, 231, 749.
- [28] L. Gross, C. Seidel, H. Fuchs, *Org. Electron.* **2002**, 3, 1.
- [29] P. Studer, S. R. Schofield, G. Lever, D. R. Bowler, C. F. Hirjibehedin, N. J. Curson, *Phys. Rev. B* **2011**, 84, 041306.
- [30] W. Höslér, W. Moritz, *Surf. Sci.* **1986**, 175, 63.
- [31] C. Nagl, E. Platzgummer, O. Haller, M. Schmid, P. Varga, *Surf. Sci.* **1995**, 331–333, 831.
- [32] A. A. Saranin, A. V. Zotov, M. Kishida, Y. Murata, S. Honda, M. Katayama, K. Oura, D. V. Gruznev, A. Visikovskiy, H. Tochiara, *Phys. Rev. B* **2006**, 74, 035436.
- [33] M. C. Militello, S. J. Simko, *Surf. Sci. Spectra* **1994**, 3, 387.